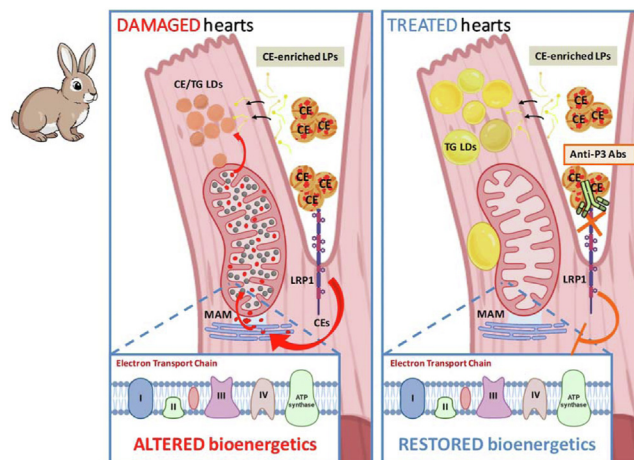


# LRP1 immunotherapy enhances cardiomyocyte respiration by restricting cholesteryl ester accumulation in mitochondria

A. Benitez-Amaro<sup>1,2</sup>, E. Garcia<sup>1,2,3</sup>, M. T. LaChica Lhoest<sup>1,2,4</sup>, A. Polishchuk<sup>1,2</sup>, I. Zegri-Reiriz<sup>5</sup>, D. Vilades<sup>5,6</sup>, J. M. Guerra<sup>5,6</sup>, L. Fernández-del-Río<sup>7,8</sup>, S. Mirabet<sup>5,6</sup>, V. Samouillan<sup>9</sup>, O. Shirihai<sup>7,8</sup>, M. Liesa<sup>10,11</sup>, C. Enrich<sup>12,13</sup>, and V. Llorente-Cortés<sup>1,2,6,\*</sup>

<sup>1</sup>Lipids and Cardiovascular Pathology Group, Biomedical Research Institut of Barcelona, IIBB-CSIC, Barcelona, Spain; <sup>2</sup>Institut de Recerca Sant Pau (IR SANT PAU), Barcelona, Spain; <sup>3</sup>Department of Medicine, Universitat Autònoma de Barcelona, Barcelona, Spain; <sup>4</sup>Departamento de Bioquímica y Biología Molecular, Universitat Autònoma de Barcelona, Barcelona, Spain; <sup>5</sup>Department of Cardiology, Hospital de la Santa Creu i Sant Pau, Institut de Recerca Sant Pau (IR SANT PAU), Universitat Autònoma de Barcelona, Barcelona, Spain; <sup>6</sup>CIBERCV, Institute of Health Carlos III, Madrid, Spain; <sup>7</sup>Department of Medicine, Endocrinology, and Department of Molecular and Medical Pharmacology, David Geffen School of Medicine, University of California, Los Angeles, CA; <sup>8</sup>Metabolism Theme, David Geffen School of Medicine, University of California, Los Angeles, CA; <sup>9</sup>CIRIMAT, Université de Toulouse, Université Paul Sabatier, Equipe PHYPOL, Toulouse, France; <sup>10</sup>Institut de Biologia Molecular de Barcelona, IIBM, CSIC, Barcelona, Spain; <sup>11</sup>CIBERDEM Institute of Health Carlos III, Madrid, Spain; <sup>12</sup>Unitat de Biologia Cel·lular, Departament de Biomedicina, Facultat de Medicina i Ciències de la Salut, Universitat de Barcelona, Barcelona, Spain; and <sup>13</sup>Centre de Recerca Biomèdica CELLEX, Institut d'Investigacions Biomèdiques August Pi i Sunyer (IDIBAPS), Barcelona, Spain

**Abstract** Antibodies (Abs) targeting the P3 sequence (Gly<sup>1127</sup>-Cys<sup>1140</sup>) of LDL receptor-related protein 1 (anti-P3 Abs) inhibit the interaction between ApoB100 in cholesteryl ester (CE)-enriched lipoproteins and the CR9 domain in LDL receptor-related protein 1, preventing intracellular CE accumulation induced by a high-fat high-cholesterol (HFHC) diet in cardiomyocytes. This study examines (i) whether HFHC induces cholesterol accumulation in mitochondria, and impacts cardiac bioenergetics, and (ii) the effectiveness of anti-P3 Abs in mitigating HFHC-induced mitochondrial alterations. Cardiac tissue was homogenized, and mitochondria were isolated through subcellular fractionation. Thin layer chromatography demonstrated that HFHC induced the accumulation of CE in cardiac mitochondria, and that this process was significantly reduced by anti-P3 Abs. In line, transmission electron microscopy studies revealed that morphological changes induced by HFHC in cardiomyocyte mitochondria were reversed, at least in part, by anti-P3 Abs. Additionally, anti-P3 Abs promoted more extensive interactions between mitochondria and lipid droplets (LDs), accompanied by an increase in LD diameter and electrodensity in cardiomyocytes. Cardiac mitochondrial respiratory capacity assessed by Seahorse analysis showed that HFHC reduced CI/CIV and CII/CIV activity ratios, while anti-P3 Abs restored complex II/IV activity. In conclusion, by blocking CE uptake from lipoproteins, anti-P3 Abs reduce CE accumulation in the cardiomyocyte mitochondria and LDs, enhance



bioenergetically favorable mitochondria/LD interactions, and improve cardiomyocyte respiratory function in hypercholesterolemic rabbits. These findings highlight the therapeutic potential of anti-P3 Abs in metabolic diseases by limiting CE loading of mitochondria and LDs in the heart and restoring cardiac bioenergetics.

Supplementary key words cholesteryl esters • heart • lipid droplets • LRP1 • mitochondria • respirometry

\*For correspondence: V. Llorente-Cortés, [Vicenta.llorente@iibb.csic.es](mailto:Vicenta.llorente@iibb.csic.es) or [cllorente@santpau.cat](mailto:cllorente@santpau.cat).

Cardiovascular disease is the leading cause of death globally. Cardiac dysfunction is marked by reduced mitochondrial respiratory capacity that disrupts cardiac metabolism and energy production (1). Research across experimental, preclinical, and clinical studies shows that mitochondrial dysfunction and bioenergetic insufficiency are key drivers in the onset (2) and progression of cardiac dysfunction (3). Cardiomyocytes are among the most mitochondria-rich cells in mammals, with mitochondria occupying over 25–30% of their volume (4, 5).

Mitochondrial function relies on coordination with other organelles, especially the endoplasmic reticulum (ER). Mitochondria-associated ER membranes (MAMs) are structural connections essential for phospholipid synthesis, intracellular transport,  $\text{Ca}^{2+}$  signaling, and maintaining mitochondrial structure, bioenergetics, and dynamics (6). Mitochondria also interact with lipid droplets (LDs); those attached to LDs, known as peridroplet mitochondria (PDM), exhibit distinct bioenergetics and dynamics compared to cytoplasmic mitochondria. PDMs show enhanced bioenergetics, including increased ATP synthesis and glucose oxidation capacity (7–9).

Lipoproteins are an essential source of fatty acids for the heart (10, 11). However, excessive low-density lipoprotein (LDL) cholesterol can impair left ventricular function by increasing left ventricular mass, as shown in a Mendelian randomization study of 17,311 European individuals (12). Both LDL and VLDLs significantly alter calcium dynamics, signal transmission, and the expression of sarcoplasmic/ER  $\text{Ca}^{2+}$ -ATPase and connexins in cultured cardiomyocytes (13–16). Additionally, cholesterol-rich diets increase ventricular susceptibility to fibrillation in rabbits, likely due to higher cholesterol content in the sarcoplasmic reticulum (17, 18). These findings underscore cholesterol buildup in cardiomyocytes as a key contributor to cardiac damage.

Intracellular cholesterol trafficking involves the mitochondria, where cholesterol buildup can lead to pathological changes, such as disrupted oxygen homeostasis, reduced antioxidant defenses, and impaired respiratory supercomplex assembly—particularly in hepatic and neurodegenerative diseases (19–23). The potential transport of exogenous dietary cholesteryl esters (CEs) to cardiomyocyte mitochondria, however, remains unexplored.

The LDL receptor-related protein 1 (LRP1) is a key receptor for the uptake of CE-rich lipoproteins in cardiomyocytes and plays a major role in CE accumulation within LDs, as shown in both *in vitro* (15, 16) and *in vivo* models (24, 25). Our group has developed an LRP1 (P3)-based immunotherapy that induces anti-P3 antibodies (Abs) to specifically block LRP1's interaction with CE-enriched lipoproteins. These antibodies effectively reduce intracellular CE accumulation without impacting triglyceride levels in cardiomyocytes (24–27). By targeting CE buildup, anti-P3 Abs restore insulin signaling (24)

and inhibit extracellular matrix (ECM) remodeling (25) in the rabbit heart model used in this study. Anti-P3 Abs offer a unique opportunity to examine the specific impact of CE accumulation on cardiac mitochondrial structure and function. The primary objectives of this study are 1) to determine whether CEs accumulate within cardiomyocyte mitochondria; 2) to assess the effects of CE accumulation on mitochondrial morphology, mitochondria/LD interactions and respiratory function; and 3) to evaluate the effectiveness of anti-P3 Abs in mitigating mitochondrial and respiratory alterations induced by CE-enriched lipoproteins.

## MATERIAL AND METHODS

### Ethics statement, study design, and animal model description

Experimental procedures were approved by the Ethics Committee of Animal Experimentation at the Vall d'Hebron Institute of Research (registration number 46/17) and conducted in accordance with Spanish legislation and European Union directives (2010/63/EU). As shown in **Figure 1**, animals were acclimated for 1 week before the initial immunization, followed by immunizations every 21 days with a primary injection and four booster doses (R1–R4). Rabbits were divided into two groups: one received an irrelevant peptide (IrP) (control group;  $n = 10$ ), and the other received P3 (treated group;  $n = 10$ ), both conjugated to the carrier. The four doses of IrP or P3 antigen, conjugated with keyhole limpet hemocyanin, were administered subcutaneously (138  $\mu\text{g}/\text{kg}$ , maximum volume 150  $\mu\text{l}$ ). For the first immunization, IrP or P3-keyhole limpet hemocyanin peptides were emulsified in complete Freund's adjuvant; subsequent immunizations used incomplete Freund's adjuvant (both from Sigma-Aldrich). During the immunization period, animals were fed a standard chow diet. As depicted in **Figure 1**, starting at the R4 time point, female New Zealand White rabbits were divided into two dietary groups for one month: i) A standard chow diet (R-01, Granja San Bernardo), consisting of 17.3% protein, 16.7% fiber, and 3% fat, and ii) a high-fat, high-cholesterol diet (HFHC, TD.140140, Harlan), consisting of 16.7% protein, 12.4% fiber, 7.6% fat, and supplemented with 1% cholesterol. Thus, there were four groups analyzed: i) standard chow, IrP-immunized; ii) standard chow, P3-immunized; iii) HFHC, IrP-immunized; and iv) HFHC, P3-immunized. The selection of a rabbit model and female sex for this study is based on previous research examining the effects of immunotherapy on atherosclerosis. Rabbits are ideal for immunotherapy studies due to their strong immune response and size, which is suitable for investigating vascular inflammation in the aorta, the primary focus of this study. Additionally, female sex hormones may influence atherosclerosis development, aligning with the replacement, reduction, and refinement principles in research.

Throughout both prediet and postdiet phases, we monitored animal weight and measured serum levels of specific anti-P3 Abs using ELISA (24–26). All animals were euthanized, and only frozen tissues and serum samples were available to develop this last study in this experimental model. Since direct cardiac bioimaging is currently not feasible, we have evaluated NT-proBNP levels to determine whether HFHC-induced

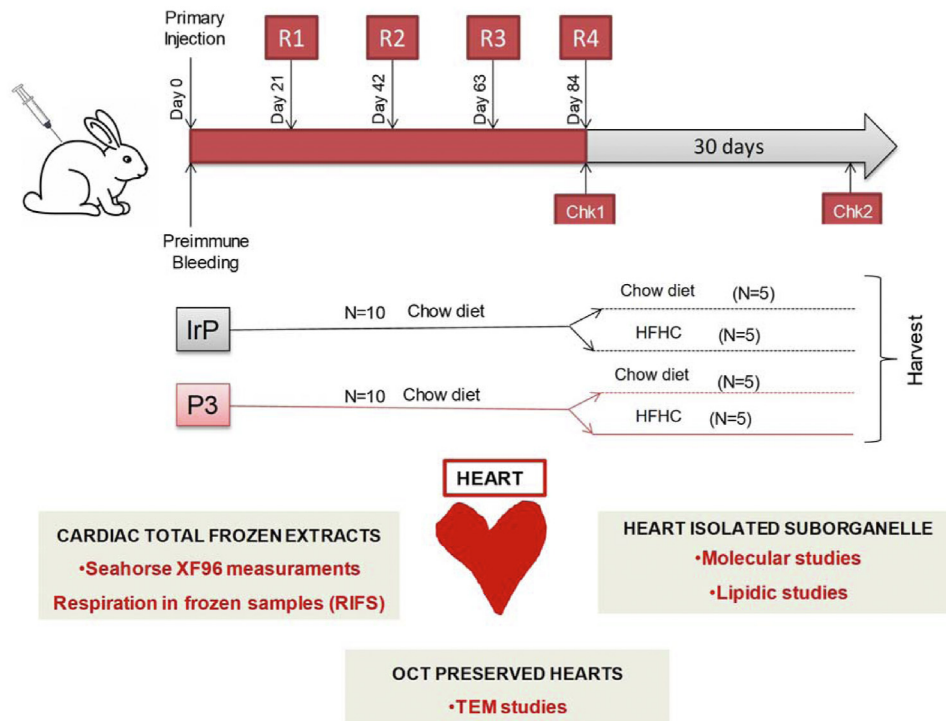


**Fig. 1.** Study Design. Rabbits were acclimated for 1 week prior to the initial immunization. They received a primary injection, followed by four booster doses (R1–R4) of either an irrelevant peptide (IrP) or P3 conjugated to a carrier protein, administered every 21 days. Baseline levels of circulating anti-P3-specific antibodies were measured at checkpoint 1 (Chk1). Starting at R4, rabbits were randomly assigned to either a normal diet or a high-fat high-cholesterol diet (HFHC) group. After 30 days on the respective diets, anti-P3 antibody levels were reassessed at checkpoint 2 (Chk2). The rabbits were then euthanized, and their hearts were collected for subcellular fractionation, molecular and lipid analyses, RIFS analysis, and transmission electron microscopy. Chk1, checkpoint 1 (prediet); Chk2, checkpoint 2 (postdiet); RIFS, respiration in frozen samples.

changes in the heart result in early (asymptomatic) or advanced (symptomatic) cardiac damage.

### Serum NT-proBNP determinations

Serum concentrations of NT-proBNP were measured using an automated electrochemiluminescence immunoassay on the Roche Cobas® e801 platform (Roche Diagnostics GmbH, Mannheim, Germany). The measuring range was 5–35,000 ng/l. Intra-assay and interassay coefficients of variation were evaluated with PreciControl cardiac 1 and 2 (Roche Diagnostics). Serum NT-proBNP levels were below 5 ng/l in all groups. This finding indicates that the cardiac changes observed in this model occur at early stages of cardiac damage.

### Peptide synthesis and conjugation

The P3 peptide used for rabbit immunization contained the sequence GDNDSDEENC, corresponding to amino acids 1,127–1,140 of the LRPI cluster II (domain CR9) (27). This sequence shows high homology between human and rabbit LRPI, with the exception that the asparagine (N) at position 1,135 in humans was replaced by a serine (S) in the rabbit protein. Additionally, the amino acid at position 1,140 in the rabbit sequence (GDNDCEDNSDEENC) was changed to cysteine (C) to enhance peptide immunogenicity. The IrP shares the same sequence as P3 but with amino acids in the D-enantiomer configuration. Both peptides were synthesized by the Laboratory of Proteomics & Protein Chemistry,

Department of Experimental & Health Sciences, Pompeu Fabra University, as previously described (27).

### Transmission electron microscopy

Rabbits were anesthetized, and their hearts were removed, immediately frozen, and embedded in OCT (Tissue-Tek, 4,583). In some experiments, small 1 mm<sup>3</sup> tissue pieces were cut and fixed in 3% glutaraldehyde with 0.1 M phosphate buffer overnight. Postfixation was carried out for 1 h at 4°C in 1% OsO<sub>4</sub> phosphate buffer. After extensive washing, the samples were dehydrated, embedded in Spurr resin, and sectioned using a Leica ultramicrotome (Leica Microsystems). Ultrathin sections (50–70 nm) were stained with 2% uranyl acetate for 10 min and with a lead-staining solution for 5 min. The sections were then examined using a JEOL JEM-1010 transmission electron microscope, equipped with a Gatan Orius SC1000 (model 832) digital camera, at the unit of electron microscopy, Scientific and Technological Centers of the University of Barcelona, School of Medicine and Health Sciences (Barcelona, Spain). Area and perimeter in LDs as well as the percentage of mitochondrial perimeter interacting with LD was analyzed in the total of mitochondrial/LD interactions observed in three ultrathin sections from each rabbit heart (n = 4 per group) using ImageJ (v. 1.51a).

### Isolation, purification, and characterization of mitochondrial fraction isolated from heart

Mitochondria and MAMs were isolated from total cardiac extracts using the method described by Wieckowski *et al.* (28).

Heart cross-sections from HFHC-fed rabbits were homogenized in an isolation buffer (225 mM mannitol, 75 mM sucrose, 0.5% BSA, 0.5 mM EGTA, and 30 mM Tris-HCl, pH 7.4) with a Dounce glass-Teflon homogenizer. The homogenate was centrifuged at 740 *g* at 4°C for 5 min to remove nuclei and unbroken cells. The supernatant was then centrifuged at 9,000 *g* for 10 min to pellet the mitochondria and MAM fractions. This pellet was washed by centrifugation at 10,000 *g* at 4°C for 10 min and subsequently resuspended in a nonionic buffer (mitochondrial resuspension buffer [MRB]) containing 250 mM mannitol, 5 mM Hepes, and 0.5 mM EGTA, pH 7.4. MAMs, and mitochondria were separated using Percoll 30% (vol/vol) density gradient centrifugation (Sigma-Aldrich, P1644) at 95,000 *g* for 30 min. Following isolation, the mitochondrial fraction was washed twice with MRB by centrifugation at 6,300 *g* for 10 min. The MAM fraction underwent a similar washing process and was then centrifuged at 100,000 *g* for 1 h. The MAM and mitochondria pellets were dissolved in MRB and quantified. The protein yield in the MAM fraction was insufficient for proper protein quantification. In contrast, the yield in the lysosomal, crude, and pure mitochondrial fractions was optimal for adequate characterization. To determine whether these isolated fractions contained contaminant membranes, we performed Western blot analysis for specific markers of lysosomes, LDs, and mitochondria in all fractions obtained from the subcellular fractionation of the heart. The following cardiac tissue sub-fractions—lysosomal, pure mitochondria, and crude mitochondria—along with total cardiac extracts, were analyzed for lysosomal-associated membrane protein 1 (LAMP1) as a lysosomal marker, perilipin 2 (PLIN2) as a LD marker, calnexin (CNX) as a MAM marker, and cytochrome C (Cyt C) and voltage-dependent anion channel (VDAC) as mitochondrial markers. Due to the large sample requirements for tissue subfractionation studies, the sample size (N) was reduced because of limited cardiac tissue availability in some animals.

### Western blot analysis

Total extract, lysosomal, crude, and pure mitochondrial fractions were analyzed using Western blotting with 10–12% SDS-PAGE gels based on their molecular weight. After separation, the proteins were transferred to a 0.45  $\mu$ m nitrocellulose membrane (Bio-Rad). The blotted proteins were probed with primary Abs against CNX (Novus Biologicals, NB100-1965SS, dilution 1 : 500), LAMP1 (Cell Signaling, #9091, dilution 1 : 1000), PLIN2 (Abcam, ab78920, dilution: 1000), VDAC (LSBIO, LS-B8743, dilution 1 : 1000), and CytC (Santa Cruz, sc-13156, dilution 1:500). Protein detection was performed using Amersham™ ECL™ Prime Western Blotting Detection Reagent (GE Healthcare) and visualized with the Chemidoc XRS system (Bio-Rad). Quantitative analysis of the results was conducted using Quantity One software (Bio-Rad).

### TLC analysis of neutral lipid content in cardiac mitochondria

Isolated mitochondrial fractions from rabbit hearts underwent neutral lipid extraction using the Bligh and Dyer method (29). The organic phase was then applied to silica chromatography plates (DC-Fertigplatten SIL G-25UV, Macherey-Nagel). Lipids were separated on the plates using an initial solvent mixture of heptane, ether, and acetic acid (72:21:4), followed by a second wash with heptane alone. The plates were stained with a solution of 5% phosphomolybdic acid and 5% sulfuric acid in ethanol and heated at 100°C for

7 min. Bands corresponding to CEs, triglycerides (TGs), and free cholesterol (FC) were quantified using a Chemidoc XRS system (Bio-Rad). To determine the amounts of CE, TG, and FC in mitochondria (ng/ $\mu$ g of mitochondrial protein), standard samples with increasing amounts ( $\mu$ g) of a mixture containing cholesterol, TGs, and cholesteryl palmitate were used (Supplemental Fig. S1). The sample data were then integrated and compared against the respective standard curves for quantification.

### Determination of gene expression by real-time PCR

Total RNA was isolated from rabbit cardiac tissue by TriPure™ isolation Reagent (Roche Molecular Biochemicals) according to the manufacturer's instructions. LRPI, classical LDL receptor (LDLR), 3-hydroxy-3-methylglutaryl-CoA reductase, and acetyl-CoA acetyltransferase 1 mRNA levels were determined by real-time PCR using the assays on demand Oc03396402\_m1, Oc03396245\_g1, Oc006714507\_m1, and Oc06778523\_m1 (Applied Biosystems), respectively. Human 18sRNA (4319413E) was used as housekeeping gene.

### Confocal microscopy studies

Heart slides were first incubated with BODIPY (5 mg/ml, 1:50 dilution, 30 min), followed by incubation with Abs against Cyt C (Santa Cruz, sc-13156, 1:50 dilution). Images of immunostained cells were viewed with HCX PL APO 63x/1.2 W Corr/0.17 CS objective in a Confocal microscope TCS SP5. Fluorescent images were acquired in a scan format of 1024  $\times$  1024 pixels in a spatial data set (xyz) and processed with the Leica Standard Software TCS-AOBS. Controls without the primary Ab showed no fluorescence labeling. For colocalization analysis, the correlation of the fluorescent signals was represented in a two-dimensional cytofluorogram, where the overlapping areas of both markers are indicated in white. A central cloud along the *y-x* axis of the cytofluorogram was selected and highlighted in white over the images. Pearson's correlation coefficient describes the correlation between intensity distributions across channels. Manders' overlap coefficient measures colocalization and indicates the extent of signal overlap, representing the degree of colocalization. The colocalization rate (CR) was calculated as the colocalized area divided by the foreground area, multiplied by 100.

### Respiration in frozen samples

The mitochondrial respiratory capacity was assessed in frozen cardiac samples using a modified protocol from Osto *et al.* (30, 31) on a Seahorse XF96 analyzer. Frozen rabbit hearts were homogenized in a mitochondria assay solution (MAS) buffer composed of 70 mM sucrose, 220 mM mannitol, 5 mM KH<sub>2</sub>PO<sub>4</sub>, 5 mM MgCl<sub>2</sub>, 1 mM EGTA, and 2 mM Hepes (pH 7.4) using a Dounce glass-Teflon homogenizer. An aliquot of the homogenate (8–12  $\mu$ g) was placed in a Seahorse XF96 microplate (103777-100) and brought to a total volume of 20  $\mu$ l with MAS buffer. The plate was centrifuged at 3,400  $\times$  rpm for 10 min at 4°C (without brake), and 130  $\mu$ l of MAS buffer containing Cyt C (100  $\mu$ g/ml) was added.

XF96 sensor cartridges were prepared with the following substrate injection sequence: NADH (1 mM) or succinate (5 mM) + rotenone (2  $\mu$ M) in port A; rotenone + antimycin A (4  $\mu$ M) in port B; N,N,N',N'-tetramethyl-p-phenylenediamine (0.5 mM) + ascorbic acid (1 mM) in port C; and azide (50 mM) in port D. NADH assessed complex I activity, succinate + rotenone evaluated complex II, and N,N,N',N'-tetramethyl-p-

phenylenediamine + ascorbic acid measured complex IV activity. Rotenone and antimycin A inhibited complexes I and II, respectively, while azide inhibited complex IV.

After preparing the microplate and cartridge, the assay was conducted on the Seahorse XF96, utilizing cycles of 2 min for mixing and 3 min for measurement, following an initial 5-min delay. The Wave software (Agilent) exported the normalized oxygen consumption rates (OCRs) per protein to GraphPad Prism v7.02. The respiratory activities of complexes I, II, and IV were calculated by subtracting the OCR values obtained with the respective activating substrates from those obtained with the inhibitors. The results are presented as the CI/CIV and CII/CIV activity ratios, as normalizing the activities of respiratory chain complexes I and II to that of complex IV is a widely recommended practice for several reasons. Complex IV (Cyt C oxidase) serves as a marker of total mitochondrial content, helping to correct for sample-to-sample variability. Additionally, this normalization ensures standardization by accounting for technical artifacts, such as differences in sample size or mitochondrial isolation efficiency. Finally, as the terminal component of the electron transport chain and essential for oxygen consumption, complex IV provides a robust functional reference for evaluating the relative activities of other complexes.

### Determination of mitochondrial content in heart homogenates

Mitochondrial content in cardiac samples was quantified using MitoTracker Deep Red (MTDR) staining. Heart homogenates (4 µg per well) were incubated with a 1 mM stock solution of MTDR diluted 1:2000 in MAS buffer. Control wells containing only buffer served as blanks. After a 10-min incubation at 37°C, the plates were centrifuged at 2000 *g* at 4°C (without brake) for 5 min, and the supernatants were carefully discarded. MAS buffer (100 µl) was added to each well, and MTDR fluorescence was measured using an excitation wavelength of 625 nm and an emission wavelength of 670 nm. Mitochondrial content was calculated as the blank-subtracted MTDR signal per milligram of protein (31).

### Statistical analysis

All results are presented as mean ± SD because the samples follow a Gaussian distribution. Statistical analyses were performed using Prism software (version 9.0, GraphPad). The normality of all variables was evaluated using the Shapiro–Wilk test. For comparisons between two groups, we employed the unpaired two-tailed Student's *t* test (for equal variances) or two-way ANOVA followed by Tukey's posthoc test (for normally distributed data with homogeneous variances). A significance level of  $P < 0.05$  was used.

Due to the high sample requirements for tissue sub-fractionation studies, the sample size (N) was reduced because of limited cardiac tissue availability from some animals. To ensure the validity of the results, we conducted a power analysis using G\*Power software, which indicated a statistical power greater than 0.8 with the current sample size.

To explore the relationships between cardiac mitochondrial lipids and biophysical ECM variables previously obtained in this model (25), we calculated Pearson's correlation coefficient (*r*) matrix using OriginPro 2023 (version 10.0.0154, OriginLab Corporation, Northampton, MA). The correlation matrix was visualized as a correlogram, with color indicating

the value of Pearson's coefficient and shape representing the confidence ellipse of scatter plots between variables. Significant correlations ( $P < 0.05$ ,  $P < 0.01$ , and  $P < 0.001$ ) were indicated with asterisks.

## RESULTS

### Mitochondrial fraction isolated from the rabbit heart is not contaminated by lysosomes or LDs but retains MAM components

Subcellular fractionation of rabbit cardiac tissue successfully yielded a fraction enriched in mitochondria, as indicated by strong positivity for VDAC and Cyt C, widely considered as mitochondrial markers. However, this fraction was not entirely free of MAM contamination, as it also tested positive for CNX, a known MAM marker. Importantly, lysosomal and LD contamination was ruled out, as the mitochondrial fraction showed no positivity for LAMP1 or PLIN2, markers of lysosomes and LDs, respectively (Fig. 2). These findings confirm that the isolated mitochondrial fraction is free from lysosomal and LD contamination but retains some MAM components. Notably, isolating a pure mitochondrial fraction from the heart appears to be more challenging than in other organs due to the high abundance of MAMs in cardiac tissue, the strong mitochondrial anchorage between myofibrils, and the tight ER-mitochondrial coupling required for calcium regulation. These characteristics are evident in the transmission electron microscopy (TEM) image presented in (Supplemental Fig. S2).

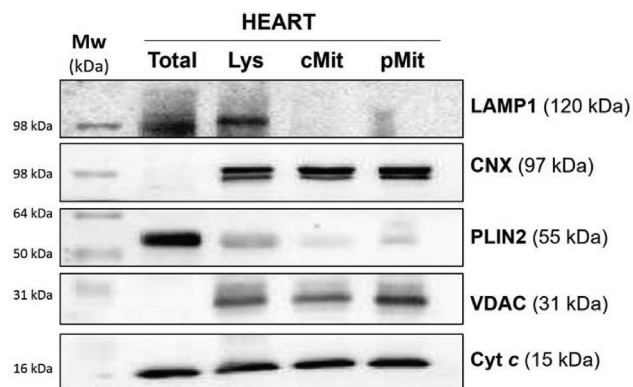


**Fig. 2.** Protein components of subcellular fractions from cardiac tissue. Cardiac tissue from hypercholesterolemic rabbits was subjected to subcellular fractionation and isolated fractions were subjected to Western blot analysis. Representative Western blot analysis showing lysosomal-associated membrane protein 1 (LAMP1) as a lysosomal marker, perilipin2 (PLIN2) as a lipid droplet marker, calnexin (CNX) as a MAM marker, and cytochrome C (Cyt C) and voltage-dependent anion channel (VDAC) as mitochondrial markers, in total cardiac extracts, and lysosomal (Lys), pure mitochondria (pMit), and crude mitochondria (cMit) subcellular fractions. The experimental procedure was performed in triplicate using pooled samples from the hearts of hypercholesterolemic rabbits. MAM, mitochondria-associated ER membrane.

## HFHC triggers CE buildup in cardiac mitochondria and disrupts cristae mitochondrial architecture

The arrival of cholesterol from CE-enriched lipoproteins to the ER led to alterations in the expression of genes involved in cholesterol metabolism. Real-time PCR revealed that LRPI receptor levels were elevated in the hearts of hypercholesterolemic rabbits compared to chow-fed rabbits (Supplemental Fig. S3A), in line with our previous findings in the vasculature of a porcine model of hypercholesterolemia (32). In addition, there was a complete reduction in cardiac levels of the classical LDLR (Supplemental Fig. S3B) and a partial decrease in HMG-CoA reductase (Supplemental Fig. S3C) levels in hypercholesterolemic rabbits, while ACAT levels remained unchanged between hyper and normocholesterolemic animals (Supplemental Fig. S3D).

Fluorometric analysis of MTDOR-stained mitochondria (Supplemental Fig. S4) and Western blot analysis of mitochondrial markers, VDAC and CytC, revealed similar mitochondrial content across all four study groups (Figs. 3A, B, and C).

The mitochondrial content of CEs, TGs, and FC was calculated based on standard curves generated with increasing doses of each lipid, as shown in Supplementary Fig. S1A–C, respectively. Thin layer chromatography (TLC) analysis of mitochondrial lipid extracts showed that CEs were undetectable in the hearts of rabbits fed a standard chow diet, while mitochondrial FC content were  $4.96 \pm 2.12$  ng FC/ $\mu$ g mitochondrial (mt) protein (Figs. 3D, E, and G). HFHC increased mitochondrial levels of CE up to  $29.68 \pm 9.54$  ng CE/ $\mu$ g mt protein ( $P < 0.001$ ) and FC levels up  $22.76 \pm 1.97$  ng FC/ $\mu$ g mt protein ( $P < 0.001$ ) in rabbit's hearts (Figs. 3D, E, and G). However, mitochondrial TG content (ng TG/ $\mu$ g mt protein) showed no significant differences between HFHC-fed ( $3.94 \pm 0.96$  ng TG/ $\mu$ g mt protein) and chow-fed rabbits ( $3.82 \pm 1.01$  ng TG/ $\mu$ g mt protein) ( $P = 0.999$ ) (Fig. 3D and F).

Confocal microscopy images revealed a high degree of colocalization between BODIPY and Cyt C in the hearts of HFHC-fed rabbits (Pearson's correlation: 0.645; overlap coefficient 0.6997; CR: 60.78%) (Fig. 4B and inset), which was not observed in standard chow-fed rabbits (Fig. 4A) (Pearson's correlation: 0.1003; overlap coefficient 0.226; CR: 8.45%).

TEM images showed that cardiomyocytes from HFHC-fed rabbits (HFHC/IrP group) had mitochondria with a tubular cristae architecture (Fig. 5B, and C), in contrast to the lamellar cristae architecture observed in mitochondria from the chow-fed group (Fig. 5A). This alteration was accompanied by signs of increased mitochondrial vacuolization and swelling (Fig. 5B, inset). Together, these results suggest that mitochondria of cardiomyocytes have been loaded with cholesterol in hypercholesterolemic rabbits.

## Anti-P3 Abs effectively inhibit CE accumulation in mitochondria and help to mitigate architectural alterations in cardiomyocytes

Immunization with P3 in this experimental model effectively increased the levels of circulating anti-P3 Abs, which significantly and selectively reduced intracellular CE accumulation in cardiomyocytes by blocking CE uptake from CE-enriched lipoproteins (24, 25). Here, TLC studies demonstrate that anti-P3 Abs efficiently inhibited CE accumulation in the mitochondria of hypercholesterolemic rabbits (P3:  $1.05 \pm 0.44$  ng CE/ $\mu$ g mt protein versus IrP:  $29.68 \pm 9.54$  ng CE/ $\mu$ g mt protein,  $P < 0.001$ ) (Fig. 3D, E). However, anti-P3 Abs did not exert any effect on mitochondrial FC levels ( $P = 0.996$ ) (Fig. 3D, G). There were no significant differences in the TG content of mitochondria (Fig. 3D, F) across the four rabbit groups. These results indicate that, in mitochondria—as in total cardiac tissue (24, 25)—anti-P3 Abs specifically reduce CE content, while having no effect on FC or TG levels.

TEM images revealed that, despite specifically reducing esterified cholesterol, anti-P3 Abs helped restore the lamellar cristae architecture in the hearts of treated rabbits (HFHC/P3 group) (Fig. 5D, D inset, 5E). The resulting mitochondrial morphology closely resembled that observed in the hearts of standard chow-fed rabbits (Fig. 5A, A inset) and was clearly distinct from that of untreated hypercholesterolemic hearts (Fig. 5B, B inset, 5C).

## Bioenergetic benefits of Anti-P3 aAbs: promoting mitochondria-LD interactions in cardiomyocytes

TEM images from rabbit heart sections revealed that LDs (white dotted rectangles) were significantly higher and more electron-dense in the cardiomyocytes of anti-P3 Ab-treated group (Fig. 6B) than the HFHC/IrP control group (Fig. 6A). Quantification of LD area and perimeter in TEM images from rabbit heart sections revealed that the LD area was  $0.19 \pm 0.09$   $\mu$ m<sup>2</sup> in the HFHC/P3 hearts, while it was  $0.06 \pm 0.05$   $\mu$ m<sup>2</sup> in the HFHC/IrP hearts ( $P < 0.001$ ) (Fig. 6C). Similarly, the LD perimeter measured  $1.57 \pm 0.41$   $\mu$ m in the HFHC/P3 hearts, compared to  $0.85 \pm 0.35$   $\mu$ m in the HFHC/IrP hearts ( $P < 0.001$ ) (Fig. 6D).

Quantitative TEM analysis illustrated two types of mitochondrial/LD contacts: a lateral interaction (Fig. 7C), which showed more extensive contact, and an apical interaction (Fig. 7A), which exhibited limited contact (white dotted rectangles). Quantification of the percentage of mitochondria involved in the contact with LD revealed that the percentage of the mitochondrial perimeter involved in lateral contact with LDs (characteristic of PDM (7, 8)) was significantly higher in the cardiomyocytes of treated hypercholesterolemic animals (HFHC/P3) (Fig. 7C, D) than untreated (HFHC/IrP) (Fig. 7A, B) as quantified in Figure 7E ( $13.33 \pm 6.97\%$  versus  $8.10 \pm 4.33\%$ ,  $P = 0.015$ ). In contrast, the percentage of mitochondrial perimeter

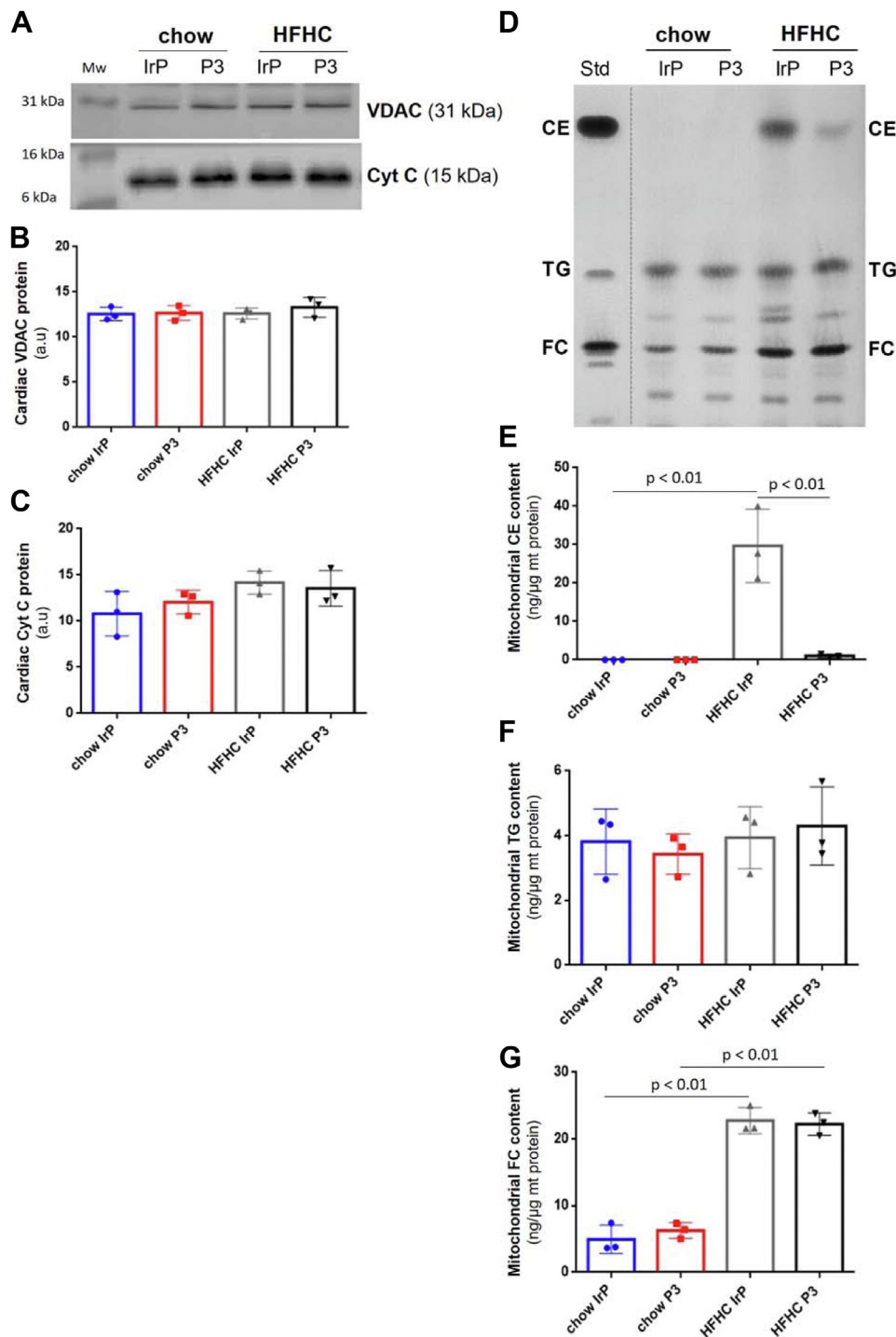


**Fig. 3.** Anti-P3 antibodies reduce cholesteryl ester content in cardiac mitochondria of hypercholesterolemic rabbits. Representative Western blot analysis (A) and bar graphs showing comparable levels of mitochondrial markers voltage-dependent anion channel (VDAC) (B) and cytochrome C (CytC) (C) across the four rabbit heart groups. D: TLC of lipid extracts from mitochondria isolated from rabbit hearts, showing bands for cholesteryl ester (CE), triglycerides (TGs), and free cholesterol (FC). Bar graphs representing the mean  $\pm$  SD of CE (E), TG (F), and FC (G) content (ng lipid/ $\mu$ g mt protein) in mitochondria isolated from the hearts of the four rabbit groups (n = 3 per group). Statistical significance was assessed using ANOVA with Tukey's posthoc test. mt, mitochondria.

involved in apical contacts with LDs (characteristic of cytoplasmic mitochondria (7, 8)) was similar in the cardiomyocytes of treated and control hypercholesterolemic rabbits ( $7.50 \pm 3.49\%$  versus  $7.21 \pm 4.37\%$ ,  $P = 0.875$ ) (Fig. 7F).

### Blocking mitochondrial CE accumulation restores complex II activity in the hearts of anti-P3-treated rabbits

In this study, we evaluated the respiratory capacity in frozen rabbit heart samples by measuring the OCR

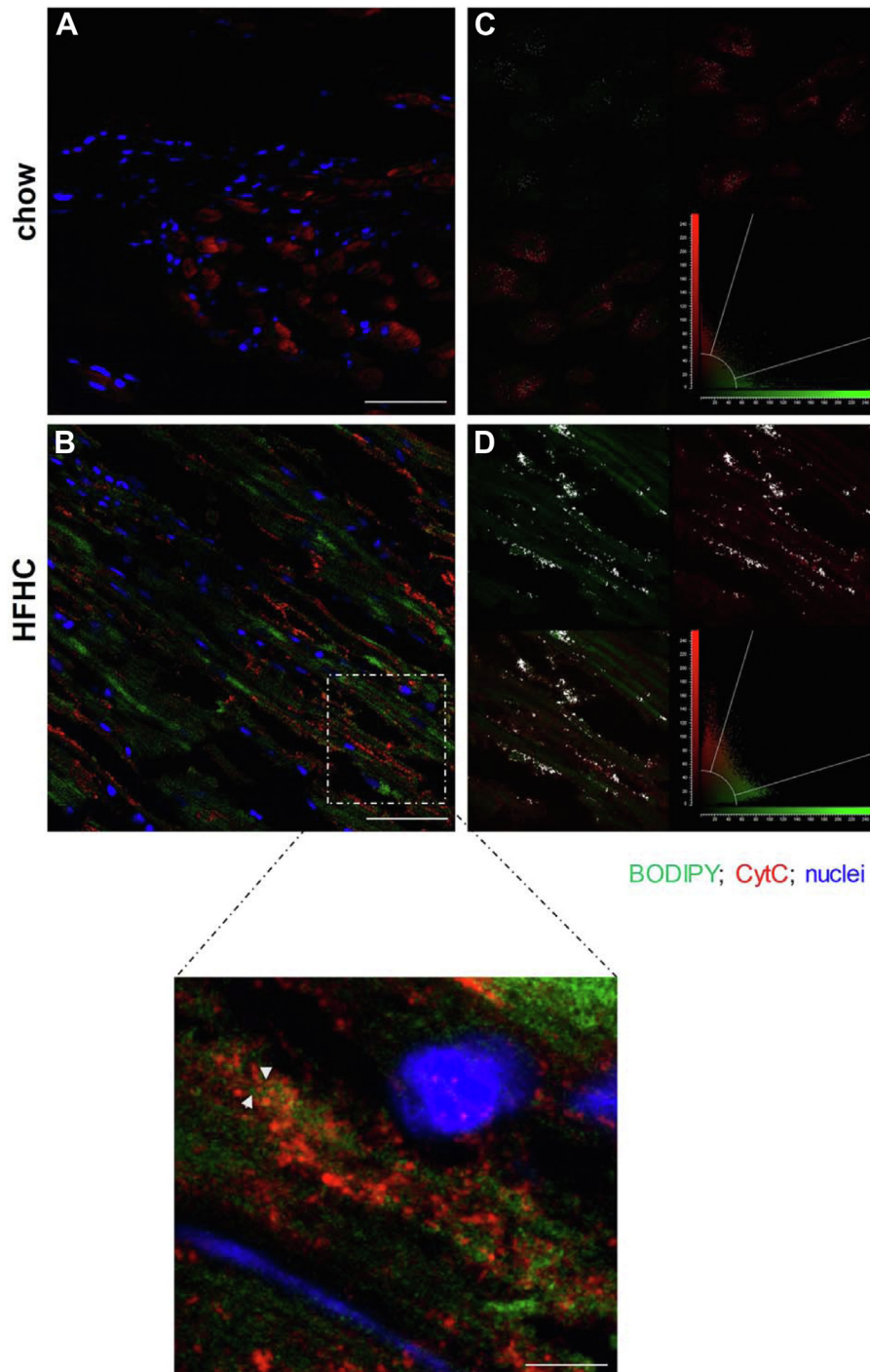


**Fig. 4.** Confocal microscopy images showing the colocalization between BODIPY and cytochrome C in the heart of hypercholesterolemic rabbits. Confocal microscopy images showing the colocalization between BODIPY (in green) and cytochrome C (in red) as yellow color in hypercholesterolemic hearts (B) but not in normocholesterolemic hearts (A). Bodipy (in green), Cyt C (in red), colocalization (in yellow), nuclei, in blue. Two-dimensional cytofluorograms showing the overlapping areas of BODIPY and Cyt C in white color in normocholesterolemic (C) and hypercholesterolemic (D) hearts. Scale: 50  $\mu\text{m}$  in A and B images; Scale: 5  $\mu\text{m}$  in the inset.

with a Seahorse XF96 Extracellular Flux Analyzer. This assessment was conducted using the innovative respirometry in frozen samples (RIFSs) protocol, following the method developed by Acín-Pérez *et al.* (30, 31). This assay allows for the analysis of the combined function of mitochondrial complexes I through IV. In frozen samples, the inner mitochondrial membrane (IMM)

becomes permeable, enabling direct access of complex I to the injected NADH. Accordingly, we observed a progressive decline in NADH-dependent OCR in rabbit heart samples (Fig. 8A), reflecting rapid NADH depletion over time, consistent with previous findings in liver samples (30). Hearts from HFHC-fed rabbits showed a significantly reduced complex I/IV activity ratio

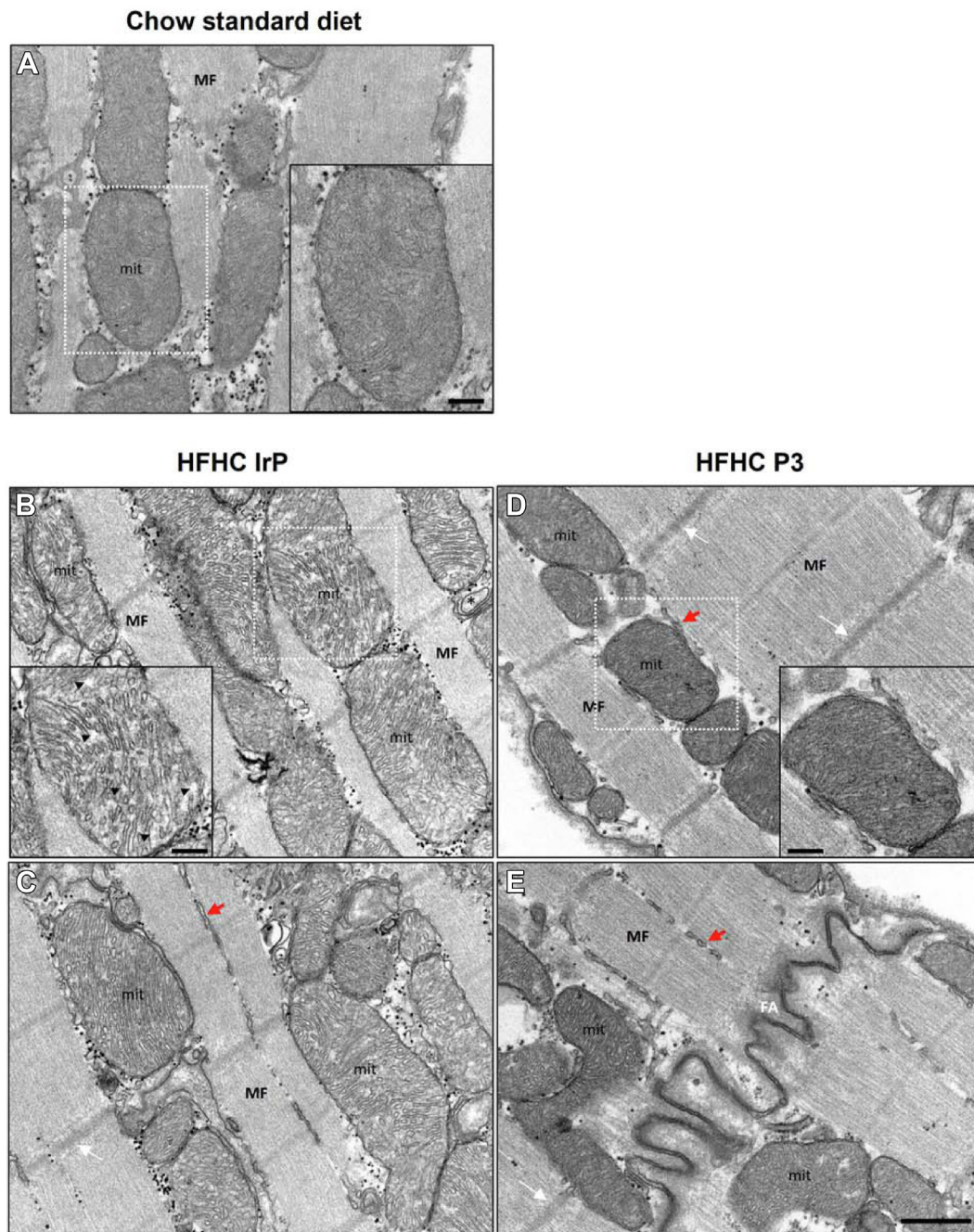


**Fig. 5.** Architecture of mitochondria in the heart of hypercholesterolemic rabbits. Comparative transmission electron microscopy (TEM) images of cardiomyocyte ultrastructure from hearts of chow standard diet (A), HFHC/IrP (B and C) and HFHC/P3 rabbits (D and E), highlighting differences in mitochondrial structure between the groups (insets from areas labeled with dotted white rectangle). Scale bar: 500 nm; inset, 220 nm. FA, fascia adherens; HFHC, high-fat high-cholesterol; IrP, irrelevant peptide; Mit, mitochondria; MF, myofibrils; white arrows, Z-bands; small red arrows, sarcoplasmic reticulum; small black arrowheads, vacuolization and tubular cristae morphology within mitochondria.

compared to those from standard chow-fed rabbits ( $0.76 \pm 0.31$  versus  $1.06 \pm 0.25$ ,  $P = 0.002$ ) (Fig. 8A, B).

To evaluate the effect of HFHC on complex II-mediated respiration, we used succinate and rotenone as substrates. Similar to the CI/CIV ratio, the CII/CIV activity ratio was significantly reduced in the hearts of HFHC compared to standard chow-fed rabbits ( $0.51 \pm 0.09$  versus  $0.71 \pm 0.25$ ,  $P = 0.010$ ) (Fig. 8C, D).

Treatment with anti-P3 Abs effectively restored the decreased cardiac CII/CIV activity ratio in hypercholesterolemic rabbits (HFHC/P3:  $0.70 \pm 0.13$  versus HFHC/IrP:  $0.51 \pm 0.09$ ,  $P = 0.003$ ) (Fig. 8C, D). However, anti-P3 treatment did not reverse the reduced CI/CIV activity ratio in hypercholesterolemic rabbits (HFHC/P3:  $0.82 \pm 0.21$  versus HFHC/IrP:  $0.76 \pm 0.31$ ,  $P = 0.913$ ) (Fig. 8A, B). These findings suggest that the reduction in

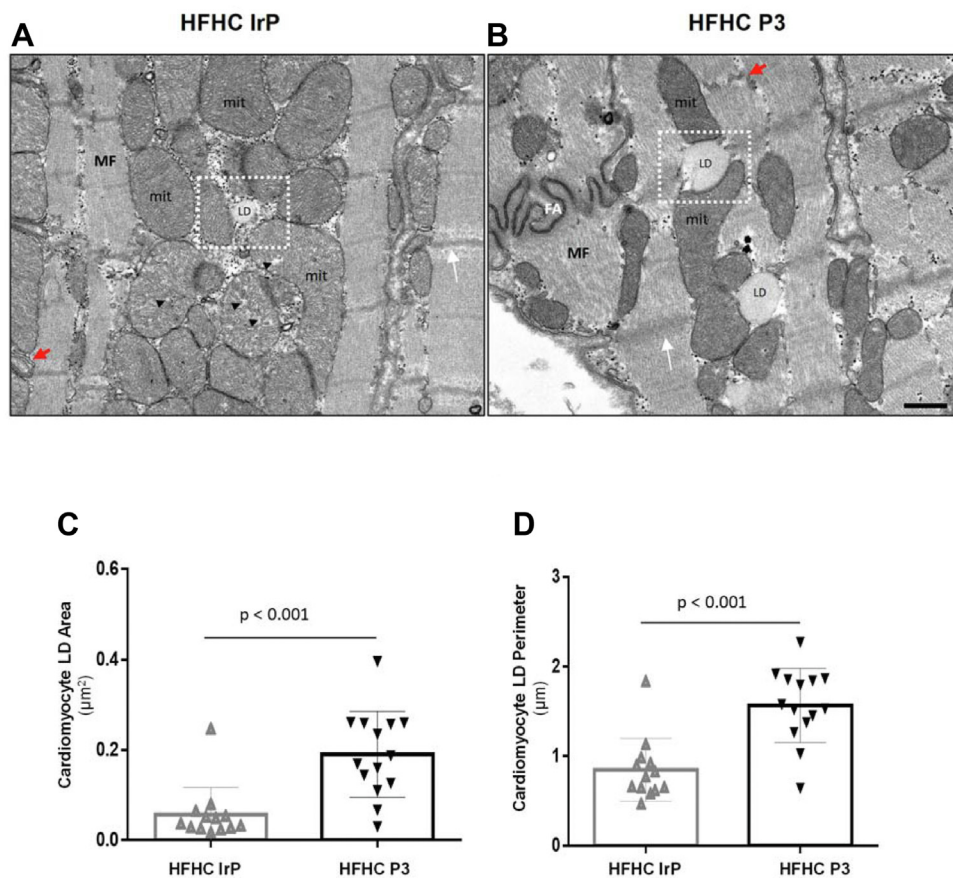


**Fig. 6.** Anti-P3 Abs increase lipid droplet size in cardiomyocytes of hypercholesterolemic rabbits. Representative TEM images of cardiomyocyte ultrastructure from hearts from HFHC/IrP (A) and HFHC/P3 (B) cardiomyocytes showing differences in LD size and electrodensity (LD differences marked in dotted white rectangles). Scale bar: 500 nm. Bar graphs showing the mean  $\pm$  SD of LD area (C) and LD perimeter (D) calculated using ImageJ (v. 1.51a) in all LDs found in 2–3 ultrathin sections from each rabbit heart ( $n = 4$ /group). Statistical significance was determined by ANOVA with Tukey's posthoc test. HFHC, high-fat high-cholesterol; IrP, irrelevant peptide; LD, lipid droplet; Mit, mitochondria; MF, myofibrils; small red arrows, sarcoplasmic reticulum; small black arrowheads, vacuolization and tubular cristae morphology within mitochondria; TEM, transmission electron microscopy.

CII/CIV, which is restored by anti-P3 Abs, is driven by mitochondrial CE (MT CE) accumulation, while the decrease in CI/CIV activity, which is unaffected by anti-P3 Abs, could be related to FC accumulation in mitochondria.

#### Mitochondrial CE accumulation is strongly associated with ECM expansion in rabbit hearts

Correlograms were generated to examine the relationships between MIT CE accumulation in the rabbit's hearts and various biophysical data previously obtained in these cardiac samples, including Fourier-transform infrared spectroscopy and thermal differential scanning calorimetry measurements (25). The correlograms indicated several significant correlations of MIT CE content with lipidic and structural biophysical variables derived from Fourier-transform infrared spectroscopy spectra of rabbit hearts (Fig. 9). MT CE exhibited strong positive correlations with cardiac total lipids ( $r = 0.857$ ,  $P < 0.001$ ), esterified lipids ( $r = 0.886$ ,  $P < 0.001$ ), and CEs ( $r = 0.778$ ,  $P < 0.005$ ). Furthermore, MIT CE was positively correlated with

morphological variables of the cardiac ECM, such as the presence of alpha helices ( $r = 0.757$ ,  $P < 0.005$ ), which are primarily found in collagen. Additionally, there were strong positive correlations with thermal differential scanning calorimetry parameters, including total water content ( $r = 0.745$ ,  $P < 0.005$ ) and bound water ( $r = 0.768$ ,  $P < 0.005$ ), indicative of ECM expansion in the heart.

## DISCUSSION

This study provides the first evidence that CE-enriched lipoproteins drive CE accumulation in mitochondria of cardiomyocytes, leading to alterations in mitochondrial morphology and bioenergetics. Notably, targeting CE accumulation with anti-P3 Abs restores mitochondrial architecture, enhances bioenergetically efficient interactions between mitochondria and LDs, and improves mitochondrial respiratory function, particularly the complex II/IV activity ratio. These findings highlight the therapeutic potential of anti-P3 Abs to counteract

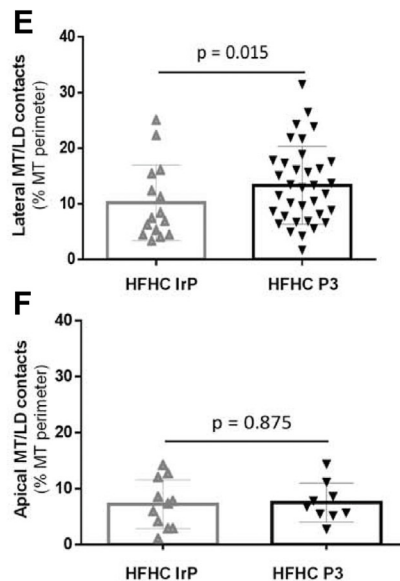
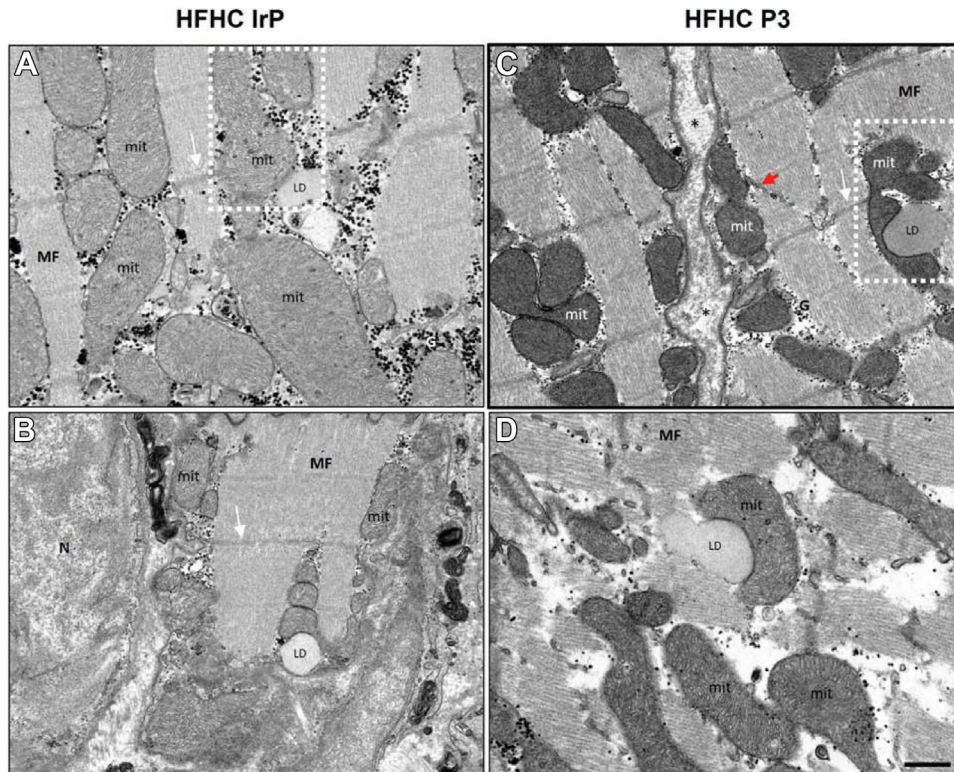


**Fig. 7.** Anti-P3 Abs increase lateral mitochondria-lipid droplet interactions in cardiomyocytes of hypercholesterolemic rabbits. Representative TEM images of cardiomyocyte ultrastructure from the hearts of HFHC/IrP (A and B) and HFHC/P3 (C and D) rabbits display differences in mitochondria-lipid droplet (LD) contacts. White dotted rectangles denote an example of lateral mitochondrial/LD contact in panel C compared to an apical mitochondrial/LD contact in panel A. Scale bar: 500 nm. Bar graphs showing the mean  $\pm$  SD of the percentage of mitochondria involved in lateral (E) and apical (F) mitochondria-LD contacts. Morphological measurements were performed using ImageJ (v. 1.51a) to calculate the percentage of the mitochondrial perimeter interacting with lipid droplets. These variables were analyzed in all mitochondria-LD contacts observed in three ultrathin sections from each rabbit heart ( $n = 4$  per group). Statistical significance was assessed by ANOVA with Tukey's posthoc test. HFHC, high-fat high-cholesterol; IrP, irrelevant peptide; LD, lipid droplet; MF, myofibrils; Mit, mitochondria; N, nuclei; TEM, transmission electron microscopy; white arrows, Z-bands; small red arrows, sarcoplasmic reticulum.

mitochondrial dysfunction in the context of hypercholesterolemia. Furthermore, a strong correlation was observed between the accumulation of MIT CE

and significant structural remodeling of the heart, most notably characterized by the expansion of the cardiac ECM.

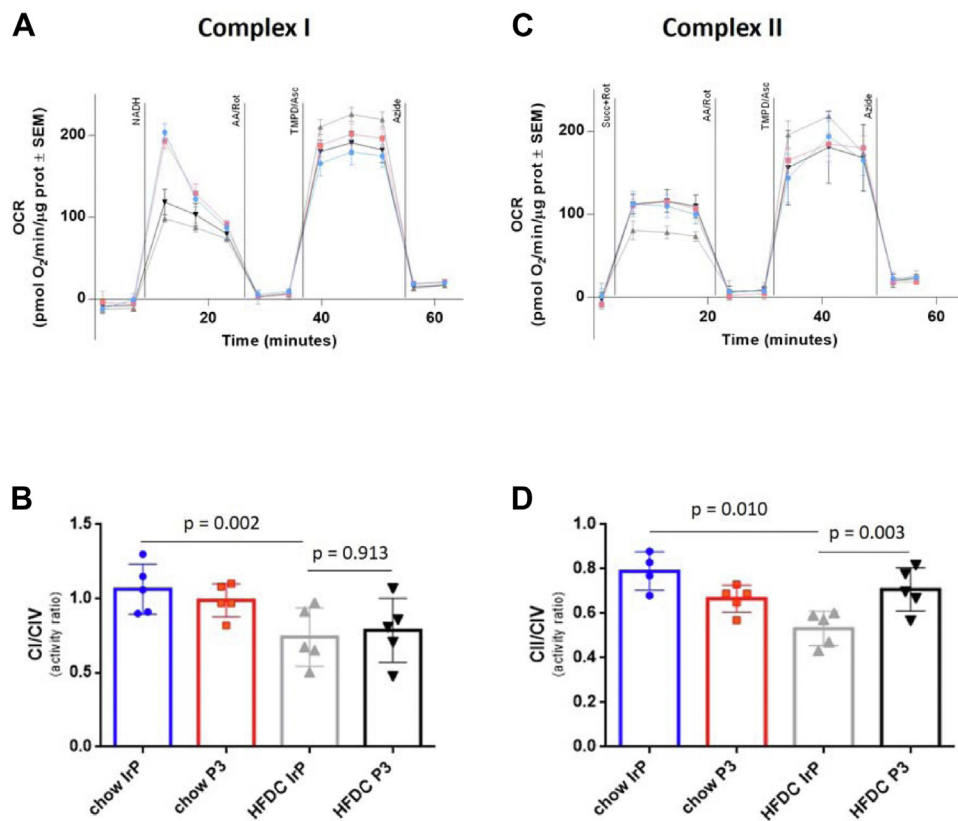


**Fig. 8.** Anti-P3 antibodies reverse the downregulatory effect of HFHC on the complex II to complex IV activity ratio. Representative NADH (A) and succinate plus rotenone (C) Seahorse profiles obtained using the RIFS respirometry protocol in cardiac homogenates from frozen rabbit hearts. Bar graphs showing the mean  $\pm$  SD of the complex I to complex IV (CI/CIV) respiratory activity ratio (B) and the complex II to complex IV (CII/CIV) respiratory activity ratio (D) in heart homogenates from the four rabbit groups. Data represent the mean  $\pm$  SD from five animals per group, with each biological replicate based on the average of four technical replicates. Statistical significance was determined by ANOVA with Tukey's posthoc test. RIFS, respirometry in frozen samples. HFHC, high-fat high cholesterol.

LDL-derived cholesterol is taken up via the LDLR and transported to the endolysosomal compartment and then transferred to the plasma membrane and ER through vesicular and nonvesicular pathways (33–38). In selective uptake pathways involving HDL, aggregated LDL, and other CE-rich lipoproteins, CE can diffuse laterally through membranes (39–42). Our group showed that LRP1 facilitates CE uptake from CE-rich lipoproteins like aggregated LDL. Using radiolabeled LDL, we found that over 90% of intracellular CE derived from agLDL uptake occurs independently of both apoB100 degradation and CE synthesis, following a nonendocytic pathway (39). This process requires the interaction between LRP1 and a specific epitope on ApoB100—distinct from the epitope that interacts with LDLR (43). These previous studies suggest that CE from CE-rich lipoproteins may reach mitochondria through nonendocytic LDL-cholesterol pathways. Currently, it remains almost completely unknown how cholesterol transported by lipoproteins reaches the mitochondria. Recently, a pioneering and outstanding study described how vesicles containing LDL and LDLR fuse with the outer mitochondrial membrane (OMM), facilitating the entry of LDL-cholesterol into the mitochondria through a process

mediated by the LDLR. Two proteins located at the OMM—phospholipase D6 and CDGSH iron-sulfur domain-containing protein 2—are essential for the fusion of LDL particles with mitochondria. CDGSH iron-sulfur domain-containing protein 2 binds to the cytosolic tail of LDLR and connects LDLR-containing vesicles to the mitochondria, while phospholipase D6 hydrolyzes cardiolipin from the OMM into phosphatidic acid, a process that facilitates the degradation of LDLR (44). Consistent with the results of this study, which show that HFHC induces CE accumulation in mitochondria, the study by Zhou *et al.* (44) and other previously described pathways—such as cholesterol transport from HDLs to the ER via the plasma membrane Aster-B pathway and subsequently to the mitochondria (45)—support the idea that CE can accumulate in mitochondria under certain conditions. The limited resolution of confocal microscopy used in this study prevents the precise localization of lipids within mitochondria in cardiomyocytes. Biophysically, it seems unlikely for CE to accumulate in the mitochondrial membranes, and it is also difficult to understand how CE could reach the mitochondrial matrix. Based on the data from this study, we cannot rule out the possibility that some CE may reside in the MAMs, as

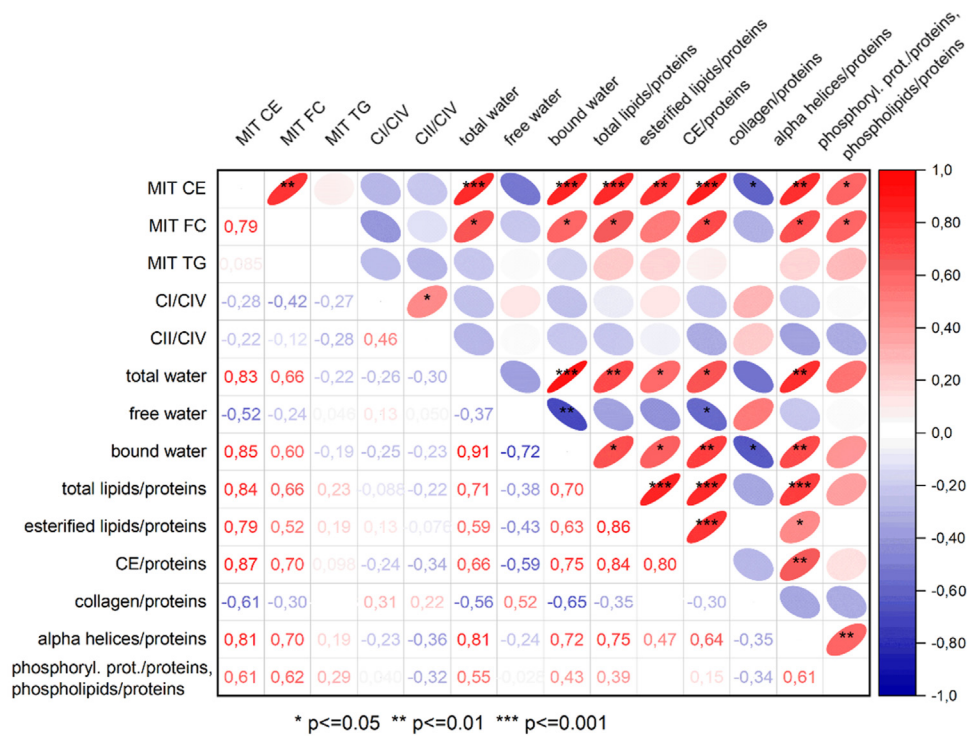


**Fig. 9.** Correlogram illustrating the positive correlation between CE accumulation in mitochondria and extracellular matrix expansion in the heart. The correlogram displays significant correlations between mitochondrial CE (MIT CE) accumulation and ECM structural variables in rabbit hearts. Positive correlations are shown in red, while negative correlations are shown in blue, with color intensity representing the strength of Pearson's correlation coefficient. The shape of each correlation is represented by a confidence ellipse derived from the scatter plot between variables. Significant correlation levels are indicated with asterisks.

the mitochondrial fraction isolated from rabbit hearts is partially contaminated by MAMs, and previous studies have reported that cholesterol transfers from the ER to mitochondria via MAMs where it can accumulate (46–48). However, the Abs that reduce CE content in mitochondria partially restore the mitochondrial cristae morphology, which is closely related to both the IMM and the mitochondrial matrix. Therefore, it cannot be excluded that CE may accumulate in the mitochondrial matrix and potentially alter IMM morphology. Additional studies using high-resolution microscopy combined with Raman spectroscopy are necessary to precisely determine CE localization within mitochondria and the morphological and functional alterations of mitochondrial cristae induced by MIT CE accumulation.

Consistent with previous studies conducted in murine liver models (19, 23), our results demonstrate that HFHC diets lead to the accumulation of FC in the mitochondria of rabbit hearts. FC, which is highly toxic to cells, is distributed among various membrane pools (49), including the subcellular membranes of organelles such as the ER and mitochondria (50–52). FC accumulated in mitochondria may derive from the hydrolysis of CE stored in LDs (45), from the ER via MAM (48), and from the plasma membrane in response to specific stimuli (46).

Based on our TEM and confocal imaging studies, the accumulation of both free and esterified forms of cholesterol may potentially participate in the pronounced shift in phenotypical mitochondrial architecture. While previous studies have highlighted the critical role of cholesterol in morphological changes in hepatic mitochondria (19), the involvement of CEs in this pathological process has not been previously reported. In this study, anti-P3 Abs, which effectively inhibit the accumulation of esterified cholesterol (CE) in cardiac mitochondria without affecting FC levels, partially recovered HFHC-induced alterations in cristae morphology in cardiomyocytes. These findings suggest that CE plays a crucial role in the disruption of mitochondrial structure. Alterations in mitochondrial cristae morphology are a hallmark of irreversible mitochondrial damage, with potentially severe consequences for ATP production (53, 54). Unlike the significant impact of HFHC on increasing MIT CE and FC content, HFHC did not appear to affect mitochondrial TG levels. The low TG levels detected in the mitochondrial fraction may be attributed to partial contamination with MAM, as these specific regions of the ER have been reported to contain TGs (55).

TEM studies from the present study provide additional evidence of HFHC-induced morphologic changes in other suborganelles such as LDs. LD area

and perimeter were increased in cardiomyocytes of treated (HFHC/P3) compared to untreated (HFHC/IrP) hearts. Our data suggest that LDs in cardiomyocytes of treated hypercholesterolemic rabbits primarily contain TGs, as the transfer of CEs from lipoproteins to LDs was inhibited by anti-P3 Abs (24). The low CE content in LDs led to a biophysical expansion of LDs in the cardiomyocytes of treated rabbits, as CEs contribute to the nucleation and packaging of LDs (56, 57). In the present study, the morphologic expansion of CE-poor LDs in cardiomyocytes of treated rabbits was associated with higher percentage of lateral LD-mitochondria contacts—characteristic of bioenergetically favorable PDMs (7–9). Our results emphasize the potential contribution of LD lipid composition on cellular mitochondrial bioenergetics. In line with our findings in cardiac tissue, recent studies in adipose and hepatic tissues have shown that LD size is a critical determinant for the bioenergetic efficiency of mitochondria/LD interactions (58). In addition to the adverse effects of MIT CE accumulation on cardiac bioenergetics reported here, previous research has indicated that intracellular CE accumulation in cardiomyocytes leads to deficiencies in myocardial insulin signaling and glucose uptake (24, 59). Collectively, these findings suggest for the first time that CE accumulation in mitochondria and LDs of cardiomyocytes significantly impact glucose and fatty acid oxidative metabolism in the heart.

RIFS experiments conducted in this study demonstrate that HFHC-induced mitochondrial cholesterol accumulation, in both free and esterified forms, contributes to the downregulation of mitochondrial respiratory activity in rabbit hearts through reduction of activities of complex I (CI) to complex IV (CIV) and complex II (CII) to CIV. This finding aligns with previous research indicating that mitochondrial cholesterol loading reduces state 3 respirations driven by complex I and complex II in the murine liver (19). Importantly, here we reported that while anti-P3 Abs restored the cardiac CII/CIV ratio, the CI/CIV ratio remained unchanged in the cardiac tissue of treated hypercholesterolemic rabbits. These results indicate that the activity of complex II (CII) in the hearts of hypercholesterolemic rabbits could be primarily affected by intracellular CE accumulation in cardiomyocyte. In contrast, complex I (CI) activity appears to be influenced by intracellular FC accumulation, which remains unchanged by anti-P3 Abs. Further research is necessary to investigate whether the restoration of CII/CIV activity by anti-P3 Abs can offset the reduction in CI/CIV activity observed in the hearts of hypercholesterolemic rabbits. Importantly, complex II (succinate dehydrogenase) serves as a critical functional link between the tricarboxylic acid cycle and oxidative phosphorylation (60).

In addition to the effects of mitochondrial CE accumulation in respiration, we found a positive correlation between mitochondrial CE accumulation and ECM expansion in rabbit hearts. Supporting our findings, other studies have shown a significant interplay between mitochondria and the ECM in various contexts, including idiopathic pulmonary fibrosis (61), cancer (62), and cartilage maintenance (63).

### Limitations of this study

One limitation of this study is that direct cardiac bioimaging is not currently feasible, as all animals were euthanized, leaving only frozen tissues and serum samples available for analysis. The evaluation of serum levels of NT-proBNP, a valuable biomarker for diagnosing heart failure and assessing cardiac stress in humans, indicated that HFHC diet induced a subclinical damage in the heart. Other limitation is that the dietary components of the standard chow and HFHC diets were not matched. Therefore, we cannot rule out the possibility that differences in fiber content between these diets may influence cholesterol absorption. It is also important to include as limitations, the partial contamination of the mitochondrial fraction by MAM and the insufficient resolution of confocal microscopy to accurately determine the localization of lipids within the mitochondria. An additional limitation is that the immunization procedure was initiated before the introduction of the HFHC, making the implementation of preventive measures in humans challenging. Furthermore, the study involved a limited number of animals per group, all of which were female. We have recently begun producing monoclonal anti-P3 Abs, and their efficacy will be evaluated using a therapeutic experimental protocol in a translational heart failure model. This approach aims to address key limitations and further advance this line of research.

### CONCLUSION

In conclusion (summarized in Fig. 10), the uptake of CE-enriched lipoproteins through the LRP1 receptor leads to CE overload of mitochondria and LDs, resulting in pathological bioenergetic changes. CE loading of LDs and mitochondria promotes unfavorable bioenergetic interactions between these organelles. MIT CE buildup also contributes to change the shape of mitochondrial cristae from lamellar to tubular. These alterations promote mitochondrial respiratory dysfunction in the heart. Anti-P3 (LRP1) Abs, which alleviate the structural and functional changes caused by CE overload in these suborganelles, improve mitochondrial respiratory function in the heart. Therefore, anti-P3 Abs present a promising therapeutic strategy for managing cardiac mitochondrial dysfunction associated with obesity, ischemia, and hypercholesterolemia—conditions known to

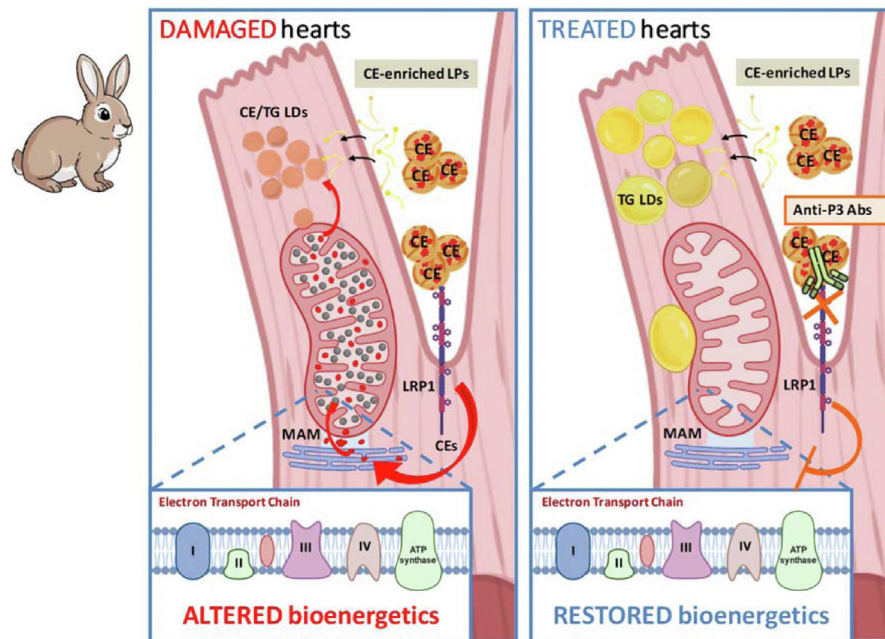


**Fig. 10.** Schematic summary of main findings. Dietary cholesterol intake results in substantial cholesteryl ester (CE) accumulation in the mitochondria and lipid droplets (LDs) of cardiomyocytes via LRP1 receptor-mediated uptake. This accumulation induces structural and functional alterations in mitochondria, LDs, and mitochondria-LD interactions, leading to impaired mitochondrial respiratory bioenergetics and extracellular matrix (ECM) remodeling in a rabbit model. Treatment with anti-P3 antibodies effectively prevents CE buildup in mitochondria and LDs, restores mitochondrial architecture, and enhances favorable lateral bioenergetic interactions between mitochondria and LDs, thereby improving mitochondrial respiratory activity. Together, these findings underscore the therapeutic potential of targeting CE accumulation in cardiomyocytes to mitigate cardiac dysfunction linked to metabolic diseases. ECM, extracellular matrix; LRP1, LDL receptor-related protein 1.

promote the accumulation of intramyocardial CE due to an altered lipoprotein profile and uptake (17, 18, 24). Despite scientific evidence linking myocardial CE accumulation to cardiac dysfunction, this phenomenon has not been clinically afforded.

### Data availability

The data, analytical methods, and study materials will be available to other researchers for purposes of reproducing the results or replicating the procedure upon reasonable request.

### Supplemental data

This article contains [supplemental data](#).

### Acknowledgments

We would like to express our gratitude to the CCI<sup>T</sup> (Campus Casanova) at the Universitat de Barcelona and Confocal Microscopy Unit of IR Sant Pau for their invaluable support in conducting Transmission Electron Microscopy and confocal microscopy studies, respectively.

### Author contributions

B.-A. A. and L. C. V. writing—original draft; B.-A. A., E. C., and L. C. V. supervision; B.-A. A., G. E., L. L. M. T., P. A., Z.-R. I., F.-d.-R. L., S. O., L. M., E. C., and L. C. V. methodology; B.-A. A., G. E., L. L. M. T., P. A., V. D., S. V., S. O., L. M., E. C., and L. C. V. investigation; B.-A. A., G. E., L. L. M. T., G. J. M., F.-d.-R. L., S. V., S. O., E. C., and L. C. V. data curation; G. E., L. L. M. T., P. A.,

G. J. M., M. S., S. O., L. M., E. C., and L. C. V. formal analysis; Z.-R. I., V. D., G. J. M., M. S., E. C., and L. C. V. validation; Z.-R. I., V. D., G. J. M., F.-d.-R. L., M. S., S. V., S. O., L. M., E. C., and L. C. V. conceptualization; S. O., E. C., and L. C. V. resources; L. C. V. funding acquisition; E. C. writing—review and editing.

### Author ORCIDs

A. Benitez-Amaro <https://orcid.org/0000-0002-1106-3125>  
M.T. LaChica Lhoest <https://orcid.org/0000-0002-9070-5973>  
D. Vilades <https://orcid.org/0000-0002-3638-9703>  
V. Samouillan <https://orcid.org/0000-0003-0571-3985>  
M. Liesa <https://orcid.org/0000-0002-5909-8570>  
V. Llorente-Cortés <https://orcid.org/0000-0002-0067-7201>

### Funding and additional information

The development of this project was financially supported by FIS PI21/01523 and FIS PI24/00618 (to VLI-C) from the Instituto de Salud Carlos III (ISCIII) and cofinanced by ERDFs, as well as by Fundación BBVA Ayudas a Equipos de Investigación 2019 (to VLI-C). B.-A. A. is a postdoctoral fellow funded by Programme Contratos Predoctorales de Formación en Investigación en Salud (FI19/00205) from ISCIII and cofinanced by ERDFs. The development of the RIFS methodology for analyzing mitochondrial respiration in frozen cardiac samples was funded by the AYUDAS PARA LA MOVILIDAD DE PERSONAL INVESTIGADOR CONTRATADO EN EL MARCO DE LA AES (M-AES) del ISCIII, granted to B.-A. A. (MV21/00060). L. L. M. T. (FPU22/01888) and G. E. (FPU21/01173) are predoctoral fellows funded by

the Spanish Ministry of Science, Innovation, and Universities in Spain. P. A. is a postdoctoral Researcher funded by CSIC through the Program “Ucrania Doctores 2022” (UCRAN 20011). Our team is part of CIBER Enfermedades Cardiovasculares (CIBERCIV; CB16/11/00276 to V.L.-C., M. S., V. D., and G. J. M.) and CIBER Diabetes y Enfermedades Metabólicas Asociadas (CIBERDEM; CB07/08/0017 to L. M.), projects run by the Instituto de Salud Carlos III. Additionally, our group participates in the Redes de Investigación (Enfermedades Metabólicas y Cáncer RED2018-102799-T), a project funded by MINECO. We are also recognized by Generalitat de Catalunya (2021 SGR 00834). The IR-SANTPAU is a center of the CERCA Programme/Generalitat de Catalunya.

#### Conflict of interest

The authors declare that they have no conflicts of interest with the contents of this article.

#### Abbreviations

Abs, antibodies; CE, cholesteryl ester; CNX, calnexin; CR, colocalization rate; Cyt C, cytochrome C; ECM, extracellular matrix; ER, endoplasmic reticulum; FC, free cholesterol; HFHC, high-fat high-cholesterol; IMM, inner mitochondrial membrane; IrP, irrelevant peptide; LAMP1, lysosomal-associated membrane protein 1; LD, lipid droplet; LDL, low-density lipoprotein; LDLR, LDL receptor; LRPI, LDL receptor-related protein 1; MAM, mitochondria-associated ER membrane; MAS, mitochondria assay solution; MRB, mitochondrial resuspension buffer; MTRD, MitoTracker Deep Red; OMM, outer mitochondrial membrane; PDM, peridroplet mitochondria; PLIN2, perilipin 2; RIFS, respiration in frozen sample; TEM, transmission electron microscopy; TG, triglyceride; TLC, thin layer chromatography; VDAC, voltage-dependent anion channel.

Manuscript received November 4, 2024, and in revised form February 25, 2025. Published, JLR Papers in Press, March 22, 2025, <https://doi.org/10.1016/j.jlr.2025.100783>

## REFERENCES

- Lopaschuk, G. D., Karwi, Q. G., Tian, R., Wende, A. R., and Abel, E. D. (2021) Cardiac energy metabolism in heart failure. *Circ. Res.* **128**, 1487–1513
- Ranjbarvaziri, S., Kooiker, K. B., Ellenberger, M., et al. (2021) Altered cardiac energetics and mitochondrial dysfunction in hypertrophic cardiomyopathy. *Circulation.* **144**, 1714–1731
- Brown, D. A., Perry, J. B., Allen, M. E., Sabbah, H. N., Stauffer, B. L., Shaikh, S. R., et al. (2017) Expert consensus document : mitochondrial function as a therapeutic target in heart failure. *Nat. Rev. Cardiol.* **14**, 238–250
- Barth, E., Stämmler, G., Speiser, B., and Schaper, J. (1992) Ultrastructural quantitation of mitochondria and myofilaments in cardiac muscle from 10 different animal species including man. *J. Mol. Cell Cardiol.* **24**, 669–681
- Ogata, T., and Yamasaki, Y. (1985) Scanning electron-microscopic studies on the three-dimensional structure of mitochondria in the mammalian red, white and intermediate muscle fibers. *Cell Tissue Res.* **241**, 251–256
- Gao, P., Yan, Z., and Zhu, Z. (2020) Mitochondria-associated endoplasmic reticulum membranes in cardiovascular diseases. *Front. Cell Dev. Biol.* **8**, 604240
- Benador, I. Y., Veliova, M., Mahdavian, K., Petcherski, A., Wikstrom, J. D., Assali, E. A., et al. (2018) Mitochondria bound to lipid droplets have unique bioenergetics, composition, and dynamics that support lipid droplet expansion. *Cell Metab.* **27**, 869–885.e6
- Benador, I. Y., Veliova, M., Liesa, M., and Shirihai, O. S. (2019) Mitochondria bound to lipid droplets: where mitochondrial dynamics regulate lipid storage and utilization. *Cell Metab.* **29**, 827–835
- Veliova, M., Petcherski, A., Liesa, M., and Shirihai, O. S. (2020) The biology of lipid droplet-bound mitochondria. *Semin. Cell Dev. Biol.* **108**, 55–64
- Basu, D., and Goldberg, I. J. (2020) Regulation of lipoprotein lipase-mediated lipolysis of triglycerides. *Curr. Opin. Lipidol.* **31**, 154–160
- Goldberg, I. J., Eckel, R. H., and Abumrad, N. A. (2009) Regulation of fatty acid uptake into tissues: lipoprotein lipase- and CD36-mediated pathways. *J. Lipid Res.* **9**, S86–S90
- Aung, N., Sanghvi, M. M., Piechnik, S. K., Neubauer, S., Munroe, P. B., and Petersen, S. E. (2020) The effect of blood lipids on the left ventricle: a mendelian randomization study. *J. Am. Coll. Cardiol.* **76**, 2477–2488
- Castellano, J., Farré, J., Fernandes, J., Bayes-Genis, A., Cinca, J., Badimon, L., et al. (2011) Hypoxia exacerbates Ca(2+)-handling disturbances induced by very low density lipoproteins (VLDL) in neonatal rat cardiomyocytes. *J. Mol. Cell Cardiol.* **50**, 894–902
- Barriga, M., Cal, R., Cabello, N., Llach, A., Vallmitjana, A., Benítez, R., et al. (2013) Low density lipoproteins promote unstable calcium handling accompanied by reduced SERCA2 and connexin-40 expression in cardiomyocytes. *PLoS One.* **8**, e58128
- Cal, R., Juan-Babot, O., Brossa, V., Roura, S., Gálvez-Montón, C., Portoles, M., et al. (2012) Low density lipoprotein receptor-related protein 1 expression correlates with cholesteryl ester accumulation in the myocardium of ischemic cardiomyopathy patients. *J. Transl. Med.* **10**, 160
- Cal, R., Castellano, J., Revuelta-López, E., Aledo, R., Barriga, M., Farré, J., et al. (2012) Low-density lipoprotein receptor-related protein 1 mediates hypoxia-induced very low density lipoprotein-cholesteryl ester uptake and accumulation in cardiomyocytes. *Cardiovasc. Res.* **94**, 469–479
- Liu, Y. B., Wu, C. C., Lu, L. S., Su, M. J., Lin, C. W., Lin, S. F., et al. (2003) Sympathetic nerve sprouting, electrical remodeling, and increased vulnerability to ventricular fibrillation in hypercholesterolemic rabbits. *Circ. Res.* **92**, 1145–1152
- Huang, Y., Walker, K. E., Hanley, F., Narula, J., Houser, S. R., and Tulenko, T. N. (2004) Cardiac systolic and diastolic dysfunction after a cholesterol-rich diet. *Circulation.* **109**, 97–102
- Solsona-Vilarrasa, E., Fucho, R., Torres, S., Nuñez, S., Nuño-Lámbardi, N., Enrich, C., et al. (2019) Cholesterol enrichment in liver mitochondria impairs oxidative phosphorylation and disrupts the assembly of respiratory supercomplexes. *Redox Biol.* **24**, 101214
- Conde de la Rosa, L., Garcia-Ruiz, C., Vallejo, C., Baulies, A., Nuñez, S., Monte, M. J., et al. (2021) STARD1 promotes NASH-driven HCC by sustaining the generation of bile acids through the alternative mitochondrial pathway. *J. Hepatol.* **74**, 1429–1441
- Singh, A., Kukreti, R., Saso, L., and Kukreti, S. (2019) Oxidative stress : a key modulator in neurodegenerative diseases. *Molecules.* **24**, 1583
- Arenas, F., Garcia-Ruiz, C., and Fernandez-Checa, J. C. (2017) Intracellular cholesterol trafficking and impact in neurodegeneration. *Front. Mol. Neurosci.* **10**, 382
- Goicoechea, L., Conde de la Rosa, L., Torres, S., García-Ruiz, C., and Fernández-Checa, J. C. (2023) Mitochondrial cholesterol : metabolism and impact on redox biology and disease. *Redox Biol.* **61**, 102643
- Actis Dato, V., Benitez-Amaro, A., Garcia, E., Claudi, L., La Chica Lhoëst, M. T., Iborra, A., et al. (2022) Targeting cholesteryl ester accumulation in the heart improves cardiac insulin response. *Biomed. Pharmacother.* **152**, 113270
- Samouillan, V., Garcia, E., Benitez-Amaro, A., La Chica Lhoëst, M. T., Dandurand, J., Actis Dato, V., et al. (2023) Inhibitory effects of LRPI-based immunotherapy on cardiac extracellular matrix biophysical alterations induced by hypercholesterolemia. *J. Med. Chem.* **66**, 6251–6262
- Bornacheva, O., Benitez-Amaro, A., Vea, A., Nasarre, L., de Gonzalo-Calvo, D., Escola-Gil, J. C., et al. (2020) Immunization with the Gly<sup>1127</sup>-Cys<sup>1140</sup> amino acid sequence of the LRPI receptor reduces atherosclerosis in rabbits. Molecular, immunohistochemical and nuclear imaging studies. *Theranostics.* **10**, 3263–3280

27. Costales, P., Fuentes-Prior, P., Castellano, J., Revuelta-Lopez, E., Corral-Rodríguez, M.Á., Nasarre, L., *et al.* (2015) Domain CR9 of low density lipoprotein (LDL) receptor-related protein 1 (LRP1) is critical for aggregated LDL-induced foam cell formation from human vascular smooth muscle cells. *J. Biol. Chem.* **290**, 14852–14865
28. Wieckowski, M. R., Giorgi, C., Lebedzinska, M., Duszynski, J., and Pinton, P. (2009) Isolation of mitochondria-associated membranes and mitochondria from animal tissues and cells. *Nat. Protoc.* **4**, 1582–1590
29. BLIGH, E. G., and DYER, W. J. (1959) A rapid method of total lipid extraction and purification. *Can. J. Biochem. Physiol.* **37**, 911–917
30. Osto, C., Benador, I. Y., Ngo, J., Liesa, M., Stiles, L., Acin-Perez, R., *et al.* (2020) Measuring mitochondrial respiration in previously frozen biological samples. *Curr. Protoc. Cell Biol.* **89**, e116
31. Acin-Perez, R., Benador, I. Y., Petcherski, A., Veliova, M., Benavides, G. A., Lagarrigue, S., *et al.* (2020) A novel approach to measure mitochondrial respiration in frozen biological samples. *EMBO J.* **39**, e104073
32. Llorente-Cortés, V., Otero-Viñas, M., Sánchez, S., Rodríguez, C., and Badimon, L. (2002) Low-density lipoprotein upregulates low-density lipoprotein receptor-related protein expression in vascular smooth muscle cells: possible involvement of sterol regulatory element binding protein-2-dependent mechanism. *Circulation.* **106**, 3104–3110
33. Kanerva, K., Uronen, R. L., Blom, T., Li, S., Bittman, R., Lappalainen, P., *et al.* (2013) LDL cholesterol recycles to the plasma membrane via a Rab8a-Myosin5b-actin-dependent membrane transport route. *Dev. Cell.* **27**, 249–262
34. Vance, J. E. (2022) Cellular itinerary of LDL cholesterol. *Proc. Natl. Acad. Sci. U. S. A.* **119**, e2122584119
35. Meneses-Salas, E., García-Melero, A., Kanerva, K., Blanco-Muñoz, P., Morales-Paytuyi, F., Bonjoch, J., *et al.* (2020) Annexin A6 modulates TBC1D15/Rab7/StARD3 axis to control endosomal cholesterol export in NPC1 cells. *Cell Mol. Life Sci.* **77**, 2839–2857
36. Höglinger, D., Burgoyne, T., Sanchez-Heras, E., Hartwig, P., Colaco, A., Newton, J., *et al.* (2019) NPC1 regulates ER contacts with endocytic organelles to mediate cholesterol egress. *Nat. Commun.* **10**, 4276
37. Lu, A. (2022) Endolysosomal cholesterol export: more than just NPC1. *Bioessays.* **44**, e2200111
38. Ikonen, E., and Olkkonen, V. M. (2023) Intracellular cholesterol trafficking. *Cold Spring Harb Perspect. Biol.* **15**, a041404
39. Llorente-Cortés, V., Otero-Viñas, M., Camino-López, S., Costales, P., and Badimon, L. (2006) Cholesteryl esters of aggregated LDL are internalized by selective uptake in human vascular smooth muscle cells. *Arterioscler Thromb. Vasc. Biol.* **26**, 117–123
40. Reaven, E., Tsai, L., and Azhar, S. (1996) Intracellular events in the "selective" transport of lipoprotein-derived cholesteryl esters. *J. Biol. Chem.* **271**, 16208–16217
41. Underwood, K. W., Jacobs, N. L., Howley, A., and Liscum, L. (1998) Evidence for a cholesterol transport pathway from lysosomes to endoplasmic reticulum that is independent of the plasma membrane. *J. Biol. Chem.* **273**, 4266–42674
42. van Meer, G., and Sprong, H. (2004) Membrane lipids and vesicular traffic. *Curr. Opin. Cell Biol.* **16**, 373–378
43. Benitez-Amaro, A., Pallara, C., Nasarre, L., Rivas-Urbina, A., Benitez, S., Veá, A., *et al.* (2019) Molecular basis for the protective effects of low-density lipoprotein receptor-related protein 1 (LRP1)-derived peptides against LDL aggregation. *Biochim. Biophys. Acta Biomembr.* **1861**, 1302–1316
44. Zhou, Y. X., Wei, J., Deng, G., Hu, A., Sun, P. Y., Zhao, X., *et al.* (2023) Delivery of low-density lipoprotein from endocytic carriers to mitochondria supports steroidogenesis. *Nat. Cell Biol.* **25**, 937–949
45. Sandhu, J., Li, S., Fairall, L., Pfisterer, S. G., Gurnett, J. E., Xiao, X., *et al.* (2018) Aster proteins facilitate nonvesicular plasma membrane to ER cholesterol transport in mammalian cells. *Cell.* **175**, 514–529.e20
46. Elustondo, P., Martin, L. A., and Karten, B. (2017) Mitochondrial cholesterol import. *Biochim. Biophys. Acta Mol. Cell Biol. Lipids.* **1862**, 90–101
47. Puglielli, L., Konopka, G., Pack-Chung, E., Ingano, L. A., Bere-zovska, O., Hyman, B. T., *et al.* (2001) Acyl-coenzyme A: cholesterol acyltransferase modulates the generation of the amyloid beta-peptide. *Nat. Cell Biol.* **3**, 905–912
48. Agrawal, R. R., Montesinos, J., Larrea, D., Area-Gomez, E., and Pera, M. (2020) The silence of the fats: a MAM's story about Alzheimer. *Neurobiol. Dis.* **145**, 105062
49. Das, A., Brown, M. S., Anderson, D. D., Goldstein, J. L., and Radhakrishnan, A. (2014) Three pools of plasma membrane cholesterol and their relation to cholesterol homeostasis. *Elife.* **3**, e02882
50. Ikonen, E. (2018) Mechanisms of cellular cholesterol compartmentalization: recent insights. *Curr. Opin. Cell Biol.* **53**, 77–83
51. Arakane, F., Sugawara, T., Nishino, H., Liu, Z., Holt, J. A., Pain, D., *et al.* (1996) Steroidogenic acute regulatory protein (StAR) retains activity in the absence of its mitochondrial import sequence: implications for the mechanism of StAR action. *Proc. Natl. Acad. Sci. U. S. A.* **93**, 13731–13736
52. Bose, H. S., Bose, M., and Whittal, R. M. (2023) Tom40 in cholesterol transport. *iScience.* **26**, 106386
53. Ježek, P., Jabůrek, M., Holendová, B., Engstová, H., and Dlasková, A. (2023) Mitochondrial cristae morphology reflecting metabolism, superoxide formation, redox homeostasis, and pathology. *Antioxid Redox Signal.* **39**, 635–683
54. Frey, T. G., and Mannella, C. A. (2000) The internal structure of mitochondria. *Trends Biochem Sci.* **25**, 319–324
55. Bassot, A., Prip-Buus, C., Alves, A., Berdeaux, O., Perrier, J., Lenoir, V., *et al.* (2021) Loss and gain of function of Grp75 or mitofusin 2 distinctly alter cholesterol metabolism, but all promote triglyceride accumulation in hepatocytes. *Biochim. Biophys. Acta Mol. Cell Biol. Lipids.* **1866**, 159030
56. Zoni, V., Khaddaj, R., Campomanes, P., Thiam, A. R., Schreiber, R., and Vanni, S. (2021) Pre-existing bilayer stresses modulate triglyceride accumulation in the ER versus lipid droplets. *Elife.* **10**, e62886
57. Shimobayashi, S. F., and Ohsaki, Y. (2019) Universal phase behaviors of intracellular lipid droplets. *Proc. Natl. Acad. Sci. U. S. A.* **116**, 25440–25445
58. Brownstein, A. J., Veliova, M., Acin-Perez, R., Villalobos, F., Petcherski, A., Tombolato, A., *et al.* (2023) Mitochondria isolated from lipid droplets of white adipose tissue reveal functional differences based on lipid droplet size. *Life Sci. Alliance.* **7**, e202301934
59. Actis Dato, V., Benitez-Amaro, A., de Gonzalo-Calvo, D., Vazquez, M., Bonacci, G., Llorente-Cortés, V., *et al.* (2020) LRP1-Mediated AggLDL endocytosis promotes cholesteryl ester accumulation and impairs insulin response in HL-1 cells. *Cells.* **9**, 182
60. Bezawork-Geleta, A., Rohlena, J., Dong, L., Pacak, K., and Neuzil, J. (2017) Mitochondrial complex II: at the crossroads. *Trends Biochem. Sci.* **42**, 312–325
61. Siekacz, K., Piotrowski, W. J., Iwański, M. A., Górski, P., and Białas, A. J. (2021) The role of interaction between mitochondria and the extracellular matrix in the development of idiopathic pulmonary fibrosis. *Oxid. Med. Cell Longev.* **2021**, 9932442
62. Romani, P., Nirchio, N., Arboit, M., *et al.* (2022) Mitochondrial fission links ECM mechanotransduction to metabolic redox homeostasis and metastatic chemotherapy resistance. *Nat. Cell Biol.* **24**, 168–180
63. Bubbs, K., Holzer, T., Nolte, J. L., *et al.* (2021) Mitochondrial respiratory chain function promotes extracellular matrix integrity in cartilage. *J. Biol. Chem.* **297**, 101224